JGR Space Physics

RESEARCH ARTICLE
10.1029/2019JA027454

The Relationship Between Cusp Region Ion Outflows and East-West Magnetic Field Fluctuations at 4,000-km Altitude

S. M. Hatch[1], T. Moretto[1], K. A. Lynch[2], K. M. Laundal[1], J. W. Gjerloev[1,3], and E. J. Lund[4]

[1]Birkeland Center for Space Science, University of Bergen, Bergen, Norway, [2]Department of Physics and Astronomy, Dartmouth College, Hanover, NH, USA, [3]The Johns Hopkins University Applied Physics Laboratory, Laurel, MD, USA, [4]Space Science Center, University of New Hampshire, Durham, NH, USA

Key Points:
- Summer/equinox outflows and east-west magnetic field fluctuations are highly correlated ($r > 0.92$)
- Winter outflows are poorer in oxygen and less correlated with magnetic field fluctuations ($r > 0.75$)
- Power indices 0.7–1.2 characterize statistical relationship between outflows and magnetic field fluctuations

Supporting Information:
- Supporting Information S1

Correspondence to:
S. M. Hatch,
Spencer.Hatch@uib.no

Citation:
Hatch, S. M., Moretto, T., Lynch, K. A., Laundal, K. M., Gjerloev, J. W., & Lund, E. J. (2020). The relationship between cusp region ion outflows and east-west magnetic field fluctuations at 4,000-km altitude. *Journal of Geophysical Research: Space Physics*, *125*, e2019JA027454. https://doi.org/10.1029/2019JA027454

Received 27 SEP 2019
Accepted 8 FEB 2020
Accepted article online 10 MAR 2020

Abstract A number of interdependent conditions and processes contribute to ionospheric-origin energetic (~10 eV to several keV) ion outflows. Due to these interdependences and the associated observational challenges, energetic ion outflows remain a poorly understood facet of atmosphere-ionosphere-magnetosphere coupling. Here we demonstrate the relationship between east-west magnetic field fluctuations (ΔB_{EW}) and energetic outflows in the magnetosphere-ionosphere transition region. We use dayside cusp region FAST satellite observations made near apogee (~4,180-km altitude) near fall equinox and solstices in both hemispheres to derive statistical relationships between ion upflow and ΔB_{EW} spectral power as a function of spacecraft frame frequency bands between 0 and 4 Hz. Identification of ionospheric-origin energetic ion upflows is automated, and the spectral power P_{EW} in each frequency band is obtained via integration of ΔB_{EW} power spectral density. Derived relationships are of the form $J_{\parallel,i} = J_{0,i} P_{EW}^{\gamma}$ for upward ion flux $J_{\parallel,i}$ at 130-km altitude, with $J_{0,i}$ the mapped upward ion flux for a nominal spectral power $P_{EW} = 1$ nT^2. The highest correlation coefficients are obtained for spacecraft frame frequencies ~0.1–0.5 Hz. Summer solstice and fall equinox observations yield power law indices $\gamma \simeq$ 0.9–1.3 and correlation coefficients $r \geq 0.92$, while winter solstice observations yield $\gamma \simeq 0.4$–0.8 with $r \gtrsim 0.8$. Mass spectrometer observations reveal that the oxygen/hydrogen ion composition ratio near summer solstice is much greater than the corresponding ratio near winter. These results reinforce the importance of ion composition in outflow models. If observed ΔB_{EW} perturbations result from Doppler-shifted wave structures with near-zero frequencies, we show that spacecraft frame frequencies ~0.1–0.5 Hz correspond to perpendicular spatial scales of several to tens of kilometers.

1. Introduction

Energetic ion outflow is a complex phenomenon within the coupled atmosphere-ionosphere-magnetosphere system that can occur via a number of multistage pathways. These stages depend on both large-scale system properties such as levels of insolation, geomagnetic and substorm activity, interplanetary magnetic field strength and orientation, solar wind parameters (Howarth & Yau, 2008; Lee et al., 2016; Moore & Horwitz, 2007; Peterson et al., 2008; Su et al., 1999; Wilson et al., 2004; Welling et al., 2015; Yau & André, 1997), and a host of more localized processes and conditions such as ambipolar electric fields, thermospheric neutral density enhancements, electron density, soft (<1 keV) electron precipitation, resonant and/or stochastic wave-particle interactions, polar cap patches, and Joule heating (André et al., 1990; Burchill et al., 2010; Kervalishvili & Lühr, 2013; Norqvist et al., 1998; Strangeway et al., 2005; Zhang et al., 2016).

Any particular instance of energetic ion outflow therefore represents interplay between a variable number of processes and conditions, which themselves vary over spatial scales ranging from tens to thousands of kilometers, over time scales ranging from seconds to years (Horwitz & Zeng, 2009; Varney et al., 2016), and with altitude (e.g., André & Yau, 1997; Bouhram et al., 2004; Fernandes et al., 2016; Nilsson et al., 2006; Nilsson, 2011; Waara et al., 2011).

Thus, complete monitoring of the energetic ion outflow process represents an enormous observational challenge, requiring in situ wave and particle observations extending from the base of the thermosphere/ionosphere through altitudes of several Earth radii into the magnetosphere.

Previous works (Strangeway et al., 2005; Zheng et al., 2005) have illustrated how covariance of putative drivers of ion upflow complicate the interpretation of the role of any particular driver. These studies nevertheless also show that drivers such as electron precipitation and Poynting flux are directly correlated with energetic ion upflow. In particular Strangeway et al. (2005), hereafter S05, reported a correlation coefficient $r = 0.721$ between average upward ion flux $\langle J_{\parallel,\mathrm{up}} \rangle$ composed predominantly of oxygen and average "DC" (i.e., spacecraft frame frequencies f_{sc} = 0–0.125 Hz) Poynting flux $\langle S_{\mathrm{DC}} \rangle$ based on measurements made during 33 Fast Auroral SnapshoT (FAST) satellite passes of the Northern Hemisphere (NH) dayside cusp region near apogee (~4,180-km altitude) in local fall equinox. Using the same 33 FAST dayside passes, Brambles et al. (2011), hereafter B11, reported a correlation coefficient $r = 0.795$ between $\langle J_{\parallel,\mathrm{up}} \rangle$ and average "AC" (f_{sc} = 0.125–0.5 Hz) Poynting flux $\langle S_{\mathrm{AC}} \rangle$. From these observations S05 and B11, respectively, derived an empirical relationship between $\langle J_{\parallel,\mathrm{up}} \rangle$ and $\langle S_{\mathrm{DC}} \rangle$, and between $\langle J_{\parallel,\mathrm{up}} \rangle$ and $\langle S_{\mathrm{AC}} \rangle$.

One likely physical explanation for the correlation between upward ion flux and Poynting flux at frequencies between 0.125 and 0.5 Hz at FAST altitudes is that this spacecraft frame frequency band is associated with Alfvén waves (Brambles et al., 2011; Hatch et al., 2017; Zhang et al., 2014). Alfvén waves are strongly associated with and can directly drive ion outflow (Chaston et al., 2006, 2007). Observational and theoretical studies show that Alfvén wave magnetic field fluctuations are primarily oriented east-west (Chaston et al., 2003; Stasiewicz et al., 2000). In addition to Alfvén waves, a variety of low-frequency wave modes and other processes observed at high latitudes have been observed to drive ion heating, upflow, and outflow (André et al., 1990, 1998; Bouhram et al., 2002; Chernyshov et al., 2017; Chugunin et al., 2018; Kintner et al., 2000; Seyler & Wahlund, 1996; Wahlund et al., 1998).

These empirical relationships, along with a similar set of relationships derived by Zheng et al. (2005) from 37 Polar satellite passes of the dayside Southern Hemisphere (SH), have either been employed directly (Brambles et al., 2010, 2011; Moore et al., 2007) or otherwise served as points of reference in ion outflow simulations and theoretical works (e.g., Brambles et al., 2011; Horwitz & Zeng, 2009; Kronberg et al., 2014; Moore & Khazanov, 2010; Varney et al., 2016). These works nonetheless all express a need for additional observational studies to validate and expand these empirical relationships. Such studies have largely not been performed, due at least in part to a lack of applicable data sets (i.e., simultaneous electric field, magnetic field, and ion distribution measurements). There are furthermore no studies demonstrating how these statistical relationships might vary with season, local time, or interplanetary magnetic field conditions. There has resultantly been only limited progress in understanding the fundamental causes and processes of ionospheric-origin ion up/outflows during the past decade (Horwitz & Zeng, 2009; Kronberg et al., 2014; Varney et al., 2016).

In this study we consider the relationship between cusp region upward ion fluxes and east-west magnetic field perturbations ΔB_{EW} in nearly arbitrary frequency bands, in both hemispheres during winter and summer. We also show that ion composition is likely an important factor in predicting energetic outflow fluxes. In section 2 we describe FAST satellite ion and magnetic field (B field) measurements and how we process these quantities to calculate average upward ion fluxes and east-west B field fluctuations as a function of spacecraft frame frequency band. We apply our methodology to the FAST observations that S05 and B11 considered and compare our results to theirs. In section 3 we use our methodology, together with four different groups of FAST observations made between December 1996 and January 1999, to obtain statistical relationships between average upward ion flux and ΔB_{EW} for nearly arbitrary spacecraft frame frequencies between 0 and 4 Hz. In section 4 we discuss and summarize the results presented in section 3, including how our methodology could be applied to current satellite missions; we discuss the role of ion composition in these as well as previous results; and we show that if we assume observed field perturbations are spatial rather than temporal, the perpendicular length scales associated with outflow near FAST apogee are of order several to a few tens of kilometers.

2. Data Set and Methodology

Launched into a polar orbit on 21 August 1996, the FAST satellite covered the range of altitudes between ~350 and 4,180 km, covering all magnetic local time (MLT) sectors every ~3 months due to the 83°

Table 1
Groups of FAST Orbits Used in This Study

Group	Section	Time period	Hemisphere	Local season	Approach[a]	N orbits
1	3.1	23–26 Sep 1998[b]	Northern	Fall	Poleward	33
2	3.2	30 Dec 1996 to 7 Jan 1997	Northern	Winter	Equatorward	38
3	3.3	8–15 Jan 1999	Southern	Summer	Poleward	32
4	3.4	24 May to 5 Jun 1998	Southern	Late Fall	Poleward	29

[a]FAST satellite direction of approach to the cusp region. [b]The group of 33 orbits used by S05 and B11.

inclination of the orbit (Carlson et al., 2001). The FAST scientific payload included a suite of instruments capable of measuring in situ magnetic and electric fields, two-dimensional electron and ion pitch angle distributions, and three-dimensional distributions of select ion species (Carlson et al., 2001; Ergun et al., 2001; Klumpar et al., 2001). Level 2 particle measurements are available for the duration of the FAST mission (ended in April 2009); Level 2 magnetic field measurements are available through October 2002 (https://cdaweb.sci.gsfc.nasa.gov/index.html/).

We use Level 1 FAST fluxgate magnetometer B field measurements and ion electrostatic analyzer (IESA) measurements of ion pitch angle distributions, which are obtained through the SDT software package (http://sprg.ssl.berkeley.edu/~sdt/SdtReleases.html).

Table 1 summarizes the four groups of FAST orbits that are used in this study. The first consists of the group of 33 NH orbits during September 1998 considered by S05 and B11. The second consists of NH observations during local winter, and the third and fourth consist of SH observations during local summer and local fall, respectively. The latter three groups of orbits were selected based on the following criteria, which mimick the characteristics of the 33 orbits used by S05 and B11:

1. Availability of ion and B field measurements over magnetic latitudes (MLats) between 60° and 87° in the NH (−87° to −60° in the SH) and over dayside MLTs;
2. Continuous ion and B field measurements at altitudes between 3,800 km and FAST apogee;
3. Satellite trajectory on the dayside that is primarily aligned with the noon-midnight meridian (as opposed to being aligned with, e.g., the dawn-dusk meridian; see Figure 1a).

MLat and MLT are defined at a reference height $h_r = 130$ km in the Modified Apex coordinate system (hereafter MA_{130}) (Laundal & Richmond, 2016; Richmond, 1995), which we obtain from the `apexpy` Python package (van der Meeren et al., 2018). In our experience, inclusion of FAST observations made under conditions not meeting requirements (1)–(3) renders the intercomparison of analysis results from each orbit group difficult or impossible. In particular relaxing the second and third requirements leads to additional sources of uncertainty/Doppler shifting of the frequencies of field measurements, as well as difference in frames of reference between FAST and ionospheric upflows that lead to sometimes overwhelming spacecraft ram ion signatures in IESA measurements. (See Heelis & Hanson, 1998; Moore et al., 1998, for some discussion of ram ions.) Thus, these requirements are imposed on orbit groups 2–4 in Table 1 to facilitate comparison with Group 1 observations, whose orbit characteristics are the basis of these requirements.

2.1. Ion Measurements and Upflow Identification Algorithm

The IESA sampled full two-dimensional ion pitch angle distributions at cadences between ~0.4 and 13 Hz, depending on the mode of operation. Figure 1a shows an example pitch angle spectrogram derived from IESA ion measurements on 25 September 1998 during FAST orbit 8276, which is the same orbit represented in Figures 1 and 2 of S05. In Figure 1a the range of pitch angles is adjusted such that "downward" (or earthward) ion measurements are correspond to the lower half ($-90° < \theta < 90°$) of the pitch angle-time spectrogram. "Upward" or (anti-earthward) ion measurements are those corresponding to the upper half ($90° < \theta < 270°$) of the pitch angle time spectrogram.

Two ion populations are visible in Figure 1a: (i) an isotropic (i.e., covering all pitch angles) magnetospheric-origin population with mirror points below the altitude of FAST, appearing between ~00:04:40 and 00:07:50 UT; (ii) an ionospheric-origin intense upflowing ion population appearing between

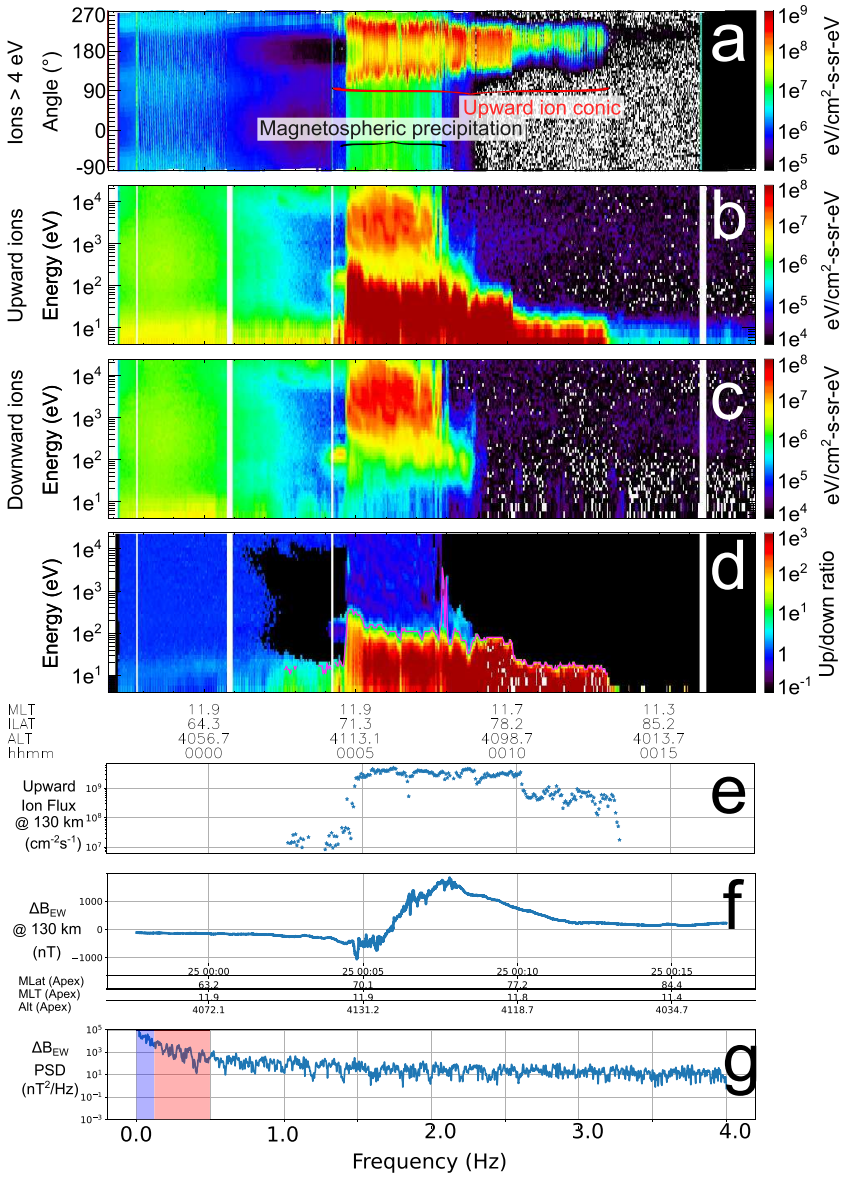

Figure 1. Ion and *B* field quantities derived from FAST observations on 25 September 1998 in the Northern Hemisphere. (a) Pitch angle spectrogram. (b) Energy spectrogram of antiearthward ("upward") ions. (c) Energy spectrogram of earthward ("downward") ions. (d) Ratio of upward and downward spectrograms in Figures 1b and 1c. (e) Upward ion energy flux after mapping to 130-km altitude. (f) ΔB_{EW} after mapping to 130-km altitude. (g) Power spectral density estimate of ΔB_{EW} time series in Figure 1f. The spacecraft frame frequency ranges termed "DC" (0–0.125 Hz) and "AC" (0.125–0.5 Hz) by S05 and B11 are highlighted in orange and blue, respectively, in Figure 1g. To avoid spuriously identifying background noise as upflow, for all energy bins in Figure 1b with upward differential energy fluxes $dJ_E/dE < 5 \times 10^5$ eV/cm^2·s·sr·eV the corresponding up/down ratio is set to zero in Figure 1d and in the upflow identification algorithm.

~00:04:40 and 00:13:30 UT, corresponding to energies between 4 and 500 eV and anti-earthward pitch angles ($90° < \theta < 270°$). In Figure 1a the ionospheric-origin population is superimposed over the isotropic magnetospheric-origin population.

Figure 1b, which is the "upward ion" energy-time spectrogram that results from averaging over antiearthward pitch angles, shows that the average differential energy fluxes of the lower-energy, ionospheric-origin ion population are intense ($dJ_E/dE \gtrsim 10^8$ eV/cm^2·s·sr·eV). This ionospheric population does not appear in the "downward ion" spectrogram (Figure 1c), which is the ion energy-time spectrogram that results from averaging over all earthward pitch angles $|\theta| < 90°$.

We wish to exclude the contribution from magnetospheric ions to the calculated ionospherically sourced upward ion flux. To achieve this, S05 and B11 manually inspected the ion energy spectrogram from each cusp pass and visually determined a cutoff energy. They then integrated the observed ion distributions up to this cutoff energy and over all pitch angles.

Attempting to exactly reproduce the results of S05 and B11 is difficult because they do not state the ion cutoff energies that were used for each orbit. We have alternatively developed the following algorithm for identification of the appropriate upper bound on ion energy.

1. For each point in time, average particle counts in each energy-angle bin over all antiearthward pitch angles to obtain an "upward ion" energy spectrogram (e.g., Figure 1b). Also average particle counts over all Earthward pitch angles to obtain a "downward ion" energy spectrogram (e.g., Figure 1c).
2. Divide the upward ion spectrogram by the downward ion spectrogram to obtain an "up/down ratio" spectrogram (Figure 1d).
3. To avoid noise, set the up/down ratio to zero for all energy bins with upward differential energy flux $dJ_E/dE < 5 \times 10^5$ eV/cm^2·s·sr·eV.
4. Let the bin with the highest energy for which the up-down ratio is at least 5 be denoted E_{top}. If either (a) no bins have an up/down ratio of at least 5, or (b) less than 75% of energy bins below E_{top} have up/down ratios of at least 1, no upflow is present in this ion distribution.
5. If the ion distribution meets the foregoing criteria, obtain the upward ion flux $J_{\|,\text{up}}$ by integrating the original two-dimensional ion distribution over all pitch angles and from the 4 eV lower limit of the IESA detector energy range up to E_{top}.

Following S05 and B11, in this study we have elected to integrate each ion distribution over all pitch angles to obtain the net ion flux. The pink line in Figure 1d indicates E_{top} as identified by this algorithm. The corresponding time series of $J_{\|,\text{up}}$ is shown in Figure 1e. All $J_{\|,\text{up}}$ are mapped to 130-km altitude (approximately the base of the F region ionosphere) via multiplication by the mapping factor $R \equiv D_i/D_{\text{FAST}} > 1$. The quantity $D = |\mathbf{d}_1 \times \mathbf{d}_2|$ is a function of the altitude-dependent basis vectors $\mathbf{d}_1$ and $\mathbf{d}_2$ in the MA_{130} coordinate system and is defined such that D_i and D_{FAST} are respectively proportional to the main-field magnitudes at 130-km altitude and at FAST altitude (Richmond, 1995). (Thus $R > 1$ for all FAST observations.) Mapped values of $J_{\|,\text{up}}$ are then averaged to obtain a single average upward ion flux.

2.2. Magnetic Field Measurements and PSD Estimates

The fluxgate magnetometer sampled all three B field components at rates between 8 and 128 Hz, depending on the mode of operation. Despinning of B field measurements is performed by the `ucla_mag_despin` routine that is included with SDT software, after which we subtract the International Geomagnetic Reference Field-12 main field model. The quantity $\Delta B_{\text{EW}} = \mathbf{e}_1 \cdot \Delta\mathbf{B}$ gives the (approximately) east-west component of the B field perturbation vector $\Delta\mathbf{B}$, where $\mathbf{e}_1$ is an MA_{130} coordinate system base vector such that ΔB_{EW} is mapped to 130 km.

Via the multitaper method (Hatch & LaBelle 2018; Slepian, 1978; Thomson, 1982), we estimate the power spectral density (PSD) of the portion of the time series that meets the MLat, MLT and altitude criteria given in section 2. We calculate the spectral power in a particular spacecraft frame frequency band by integrating the PSD estimate over all frequencies within that band. For example, a ~15-min time series of ΔB_{EW} is shown in Figure 1f, with the corresponding multitaper PSD estimate shown in Figure 1g. The spacecraft frame frequency ranges termed "DC" (0–0.125 Hz) and "AC" (0.125–0.5 Hz) by S05 and B11 are respectively highlighted in blue and orange. Integration of the PSD estimate over DC and AC frequency bands thus defined yields spectral powers of 2.88×10^5 nT^2 and 6.67×10^2 nT^2, respectively.

2.3. Comparison With S05 and B11

In summary, the methodology of S05 and B11 is based on manual identification of an ion cutoff energy for each cusp pass and average Poynting flux calculated from time series of B field and electric field measurements. In contrast, our methodology is based on automated identification of ion outflows for each cusp pass and a spectral representation of B field measurements. We now compare analysis results using each methodology to determine whether our methodology, which excludes electric field measurements and uses frequency-domain (instead of time-domain) calculations of average B field fluctuations, yields correlation coefficients that are similar to those yielded by the S05 and B11 methodology.

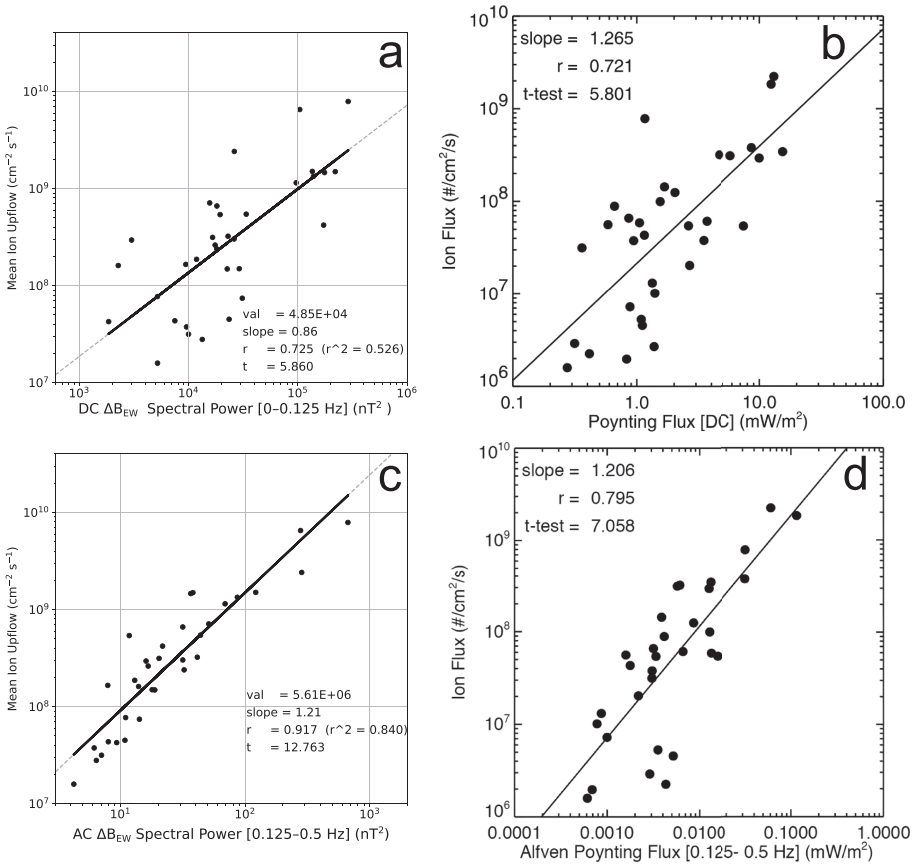

Figure 2. Scatterplots of average upward ion flux versus ΔB_{EW} spectral power (panels a and c) and Poynting flux (panels b and d) in DC (0–0.125 Hz; a and b) and AC (0.125–0.5 Hz; bottom row) spacecraft frame frequency bands for 33 NH cusp region passes in September 1998. ΔB_{EW} spectral power in DC and AC frequency bands (left column) are calculated via the methodology described in section 2.2. Poynting flux in each frequency band (right column) is calculated via the methodology of Strangeway et al. (2005) (S05). Each panel also shows the best fit line and fit parameters described in section 2.3. Figure 2b was originally presented by S05 as Figure 5. Figure 2d was originally presented by Brambles et al. (2011) (B11) as their Figure S1. They are reproduced with permission from John Wiley and Sons and the American Association for the Advancement of Science, respectively.

Figure 2 presents the scatterplots of average upward ion flux versus ΔB_{EW} spectral power in DC and AC spacecraft frame frequency bands (respectively, Figures 2a and 2c) in the left-hand column from the same 33 orbits presented by S05 and B11, and the scatterplots of average upward ion flux versus Poynting flux in DC and AC frequency bands (respectively Figures 2b and 2d) presented by S05 and B11. Each panel also shows the best fit line and fit parameters that result from performing a least squares linear fit to the logarithm of the quantities shown on the x and y axes.

In the two panels showing "DC" field fluctuations (top row in Figure 2), the correlation coefficients are very similar ($r = 0.725$ and $r = 0.721$) while the slopes differ ($\gamma = 0.85$ and $\gamma = 1.265$ in Figures 2a and 2b, respectively). In the two panels showing "AC" field fluctuations (bottom row in Figure 2), the correlation coefficients are different ($r = 0.917$ and $r = 0.795$) while the slopes are almost identical ($\gamma = 1.20$ and $\gamma = 1.206$ in Figures 2c and 2d, respectively).

From the comparison of methodologies shown in Figure 2, we conclude that our methodology yields correlation values that are comparable to or higher than those resulting from the S05 and B11 methodologies. While our methodology provides no information about which processes or possibly wave modes may be operating in association with the observed outflows, it nevertheless makes apparent that electric field measurements are not necessary for determination of an empirical relationship between field perturbations and energetic ion outflow.

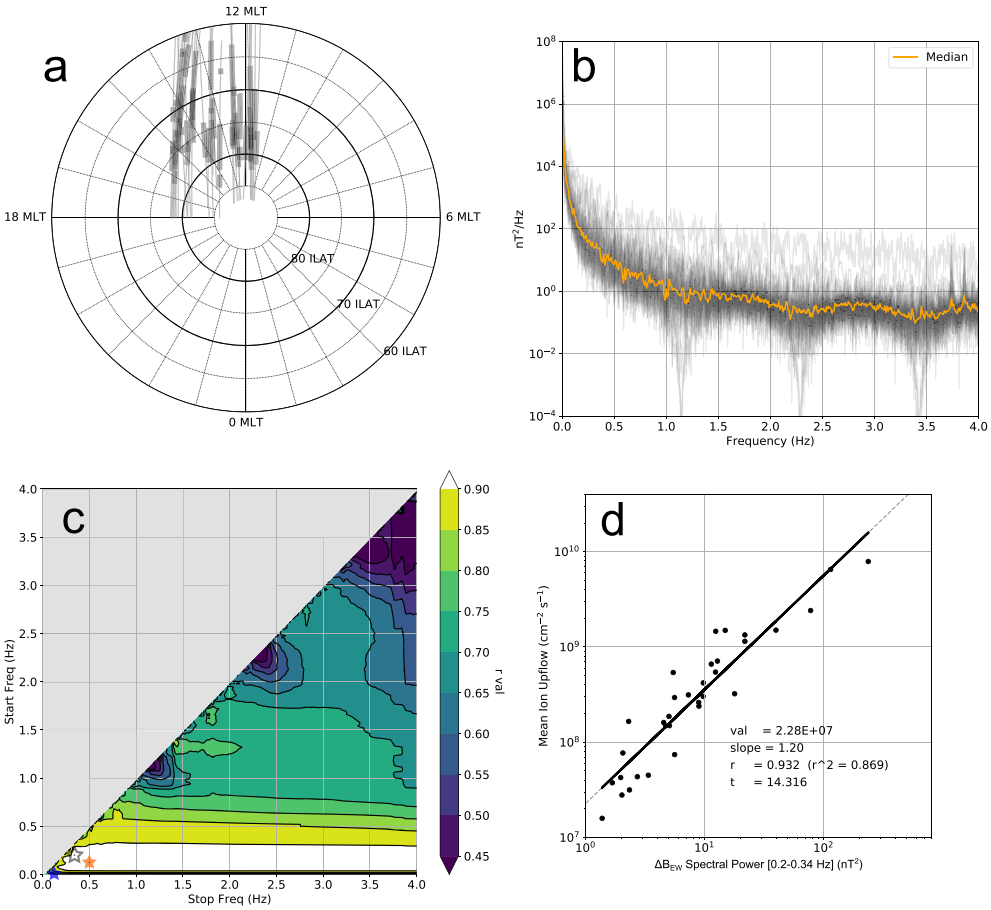

Figure 3. Ion and ΔB_{EW} statistics from 33 NH cusp region passes during 23–26 September 1998. (a) Contributing portions of orbits, where thick lines indicate identified ion outflow. (b) Individual power spectral density (PSD) estimates of ΔB_{EW} time series (black transparent lines) and median PSD (orange line). (c) Correlation coefficient r of least squares linear fit to the logarithm of average upward ion flux and logarithm of spectral power as a function of PSD start integration frequency (y axis) and stop integration frequency (x axis). (d) Least squares linear fit for spacecraft frame frequency band 0.2–0.34 Hz, which yields the highest least squares correlation coefficient r in panel c. In panel c the S05 DC and AC frequency bands as well as highest-correlation frequency band are respectively indicated by blue, orange, and transparent black stars.

We now apply our methodology to four groups of orbits to investigate the relationship between $J_{\parallel,up}$ and ΔB_{EW} as a function of season, hemisphere, and frequency band.

3. Statistical Relationships Between Ion Outflow and ΔB_{EW}

The AC and DC frequency bands defined by S05 arose in connection with the interpolation and the series of decimations and smoothings that they applied to the time series of field measurements (Appendix A in S05). In contrast the spectral method we use allows for analysis of an arbitrary frequency band, up to the frequency resolution of each PSD (typically less than 0.01 Hz).

In this section we perform the same type of correlation and fitting shown in Figure 2 for the 19,900 possible frequency bands between 0 and 4 Hz with spectral resolution 0.02 Hz, for the four groups of orbits indicated in Table 1. We hypothesize that the inferred relationship between average ion outflow and B field fluctuations varies as a function of season and hemisphere. To test this hypothesis we analyze each group of orbits separately.

3.1. Northern Hemisphere, September 1998 (Local Fall)

Figure 3 shows the results of analysis of 19,900 frequency bands between 0 and 4 Hz for the 33 NH cusp region passes considered by S05 and B11. Figure 3a shows the portion of each pass that meets the three criteria in section 2 (60–87° MLat, 6–18 MLT, and at or above 3,800-km altitude), with thick lines indicating

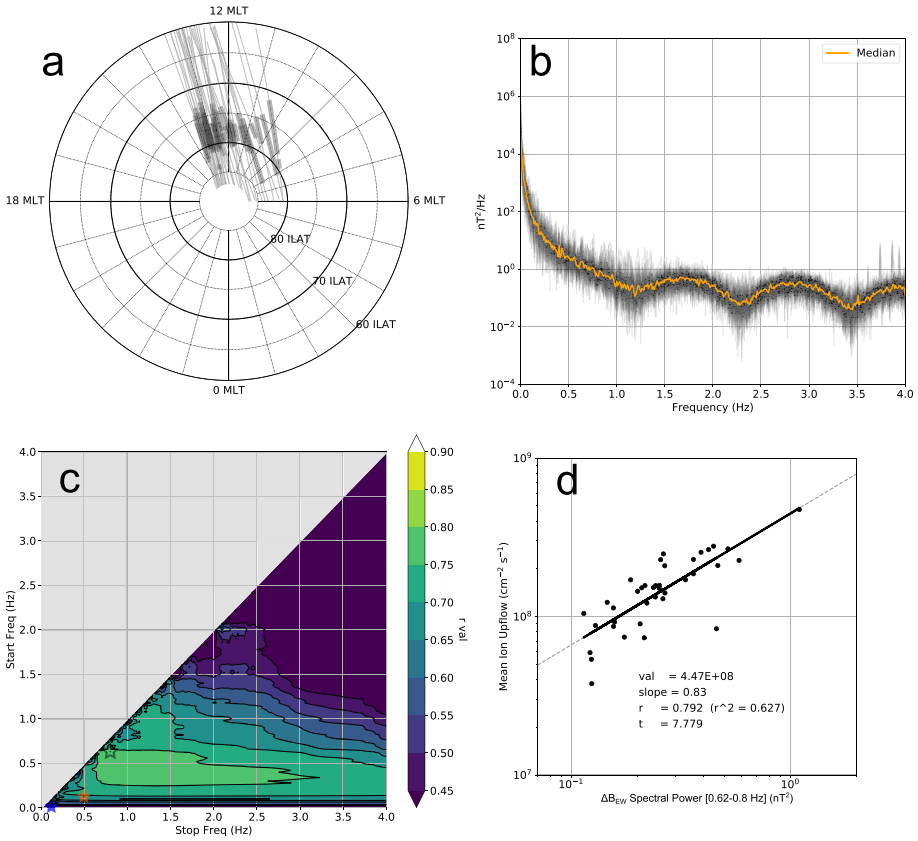

Figure 4. Ion and ΔB_{EW} statistics from 38 NH cusp region passes between 30 December 1996 and 7 January 1997. The format of all panels is identical to corresponding panels in Figure 3. (a) Portions of orbits between 60° and 87° MLat, 6–18 MLT, and at or above 3,800-km altitude. Thick lines indicate identified ion outflow. In panel (d) the spacecraft frame frequency band that yields the highest correlation coefficient is 0.62–0.8 Hz.

observations of ion outflow. Except during storms, the geomagnetic cusp is typically observed at 70° < MLat < 80° (Zhang et al., 2013; Zhou et al., 2000). The observation of ion outflows at MLat < 70° during several passes is therefore indicative of the geomagnetic storm that occurred during 24–25 September 1998.

Figure 3b shows the PSD estimate for each ΔB_{EW} time series as well as the median PSD (orange line). The median PSD ranges over nearly seven orders of magnitud, and decreases by roughly 4 orders of magnitude between 0 and ~0.2 Hz. (The two spikes that reach $\sim 10^{1.5}$ nT^2/Hz at ~3.7 and 3.9 Hz are artifacts related to the `ucla_mag_despin` routine, whereas the troughs at ~1.1, 2.35, and 3.45 Hz are related to the recursive filter of the fluxgate magnetometer (Elphic et al., 2001). Similar artifacts are visible in the PSDs shown in Figures 4b, 5b, and 6b.)

Figure 3c displays the correlation coefficient r resulting from a least squares linear fit to the logarithm of the average mapped upward ion flux and the logarithm of ΔB_{EW} spectral power within the frequency bands given by the x and y axes. The x axis gives the upper bound ("stop frequency") of the frequency band f_{top}, and the y axis gives the lower bound ("start frequency") of the frequency band f_{bot}. Each linear fit is of the form

$$\log_{10} J_{\parallel,i} = J_{0,i} + \gamma \log_{10} P_{\mathrm{EW}}, \tag{1}$$

where $J_{\parallel,i}$ is the predicted upward ion flux after mapping to 130-km altitude, γ is the power law index (Figure 3d), P_{EW} is the spectral power within the selected frequency band, and $J_{0,i}$ is the mapped upward ion flux (in cm^{-2} s^{-1}) for nominal spectral power $P_{\mathrm{EW}} = 1$ nT^2.

As an aid in the interpretation of Figure 3c, we indicate with a blue star the DC frequency band 0–0.125 Hz defined by S05, corresponding to Figures 2a and 2b. (See also the DC frequency band shaded blue in Figure 1g.) We indicate with an orange star the AC frequency band 0.125–0.5 Hz defined by S05, corresponding to Figures 2c and 2d. (See also the AC frequency band shaded orange in Figure 1g.)

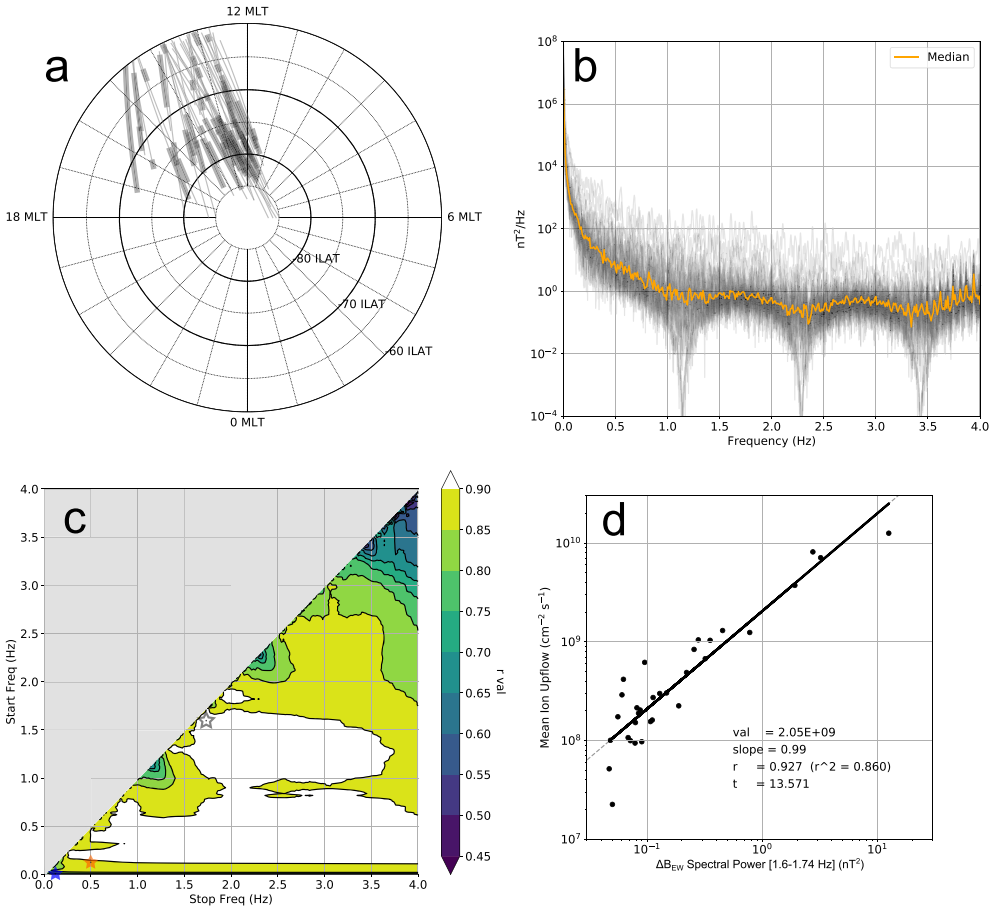

Figure 5. Ion and ΔB_{EW} statistics from 32 SH cusp region passes during 8–15 January 1999. The format of all panels is identical to corresponding panels in Figure 3. (a) Portions of orbits between −87° and −60° MLat, 6–18 MLT, and at or above 3,800-km altitude. Thick lines indicate identified ion outflow. In panel (d) the spacecraft frame frequency band that yields the highest correlation coefficient is 1.6–1.74 Hz.

The highest correlation coefficients ($r \geq 0.9$) correspond to frequency bands such that 0.08 Hz $\lesssim f_{\mathrm{bot}} \lesssim$ 0.3 Hz and $f_{\mathrm{bot}} < f_{\mathrm{top}} \lesssim$ 4 Hz. In particular the frequency band 0.2–0.34 Hz (indicated by the transparent black star in Figure 3c) yields the highest correlation coefficient $r = 0.932$, with a best fit relationship $J_{\parallel,i} = 2.28 \times 10^7 P_{\mathrm{EW}}^{1.20}$.

3.2. Northern Hemisphere, December 1996 (Local Winter)

Figure 4 shows the results of analysis of 19,900 frequency bands between 0 and 4 Hz for 38 NH cusp region passes occurring between 30 December 1996 and 7 January 1997, corresponding to local winter. The layout identical to that of Figure 3. Figure 4a shows that observed ion outflows are confined to MLat $\gtrsim$ 70° during these passes, with the majority observed at MLat $\gtrsim$ 75°. Outflows at these latitudes are indicative of the geomagnetic quiescence that prevails throughout the 9-day period.

Figure 4b shows that the individual PSD estimates (transparent black lines) and median PSD (orange line) vary less overall than the PSD estimates shown in Figure 3b. The median PSD ranges over fewer than 6 orders of magnitude, decreasing by roughly 2 orders of magnitude over 0–0.2 Hz.

In Figure 4c, the highest correlation coefficients ($r \geq 0.75$) correspond to spacecraft frame frequency bands such that 0.25 Hz$\leq f_{\mathrm{bot}} \leq$0.7 Hz and 0.6 Hz$\leq f_{\mathrm{top}} \leq$1.5 Hz. In particular the frequency band 0.62–0.8 Hz yields the highest correlation coefficient $r = 0.792$, with a best-fit relationship $J_{\parallel,i} = 4.47 \times 10^8 P_{\mathrm{EW}}^{0.83}$.

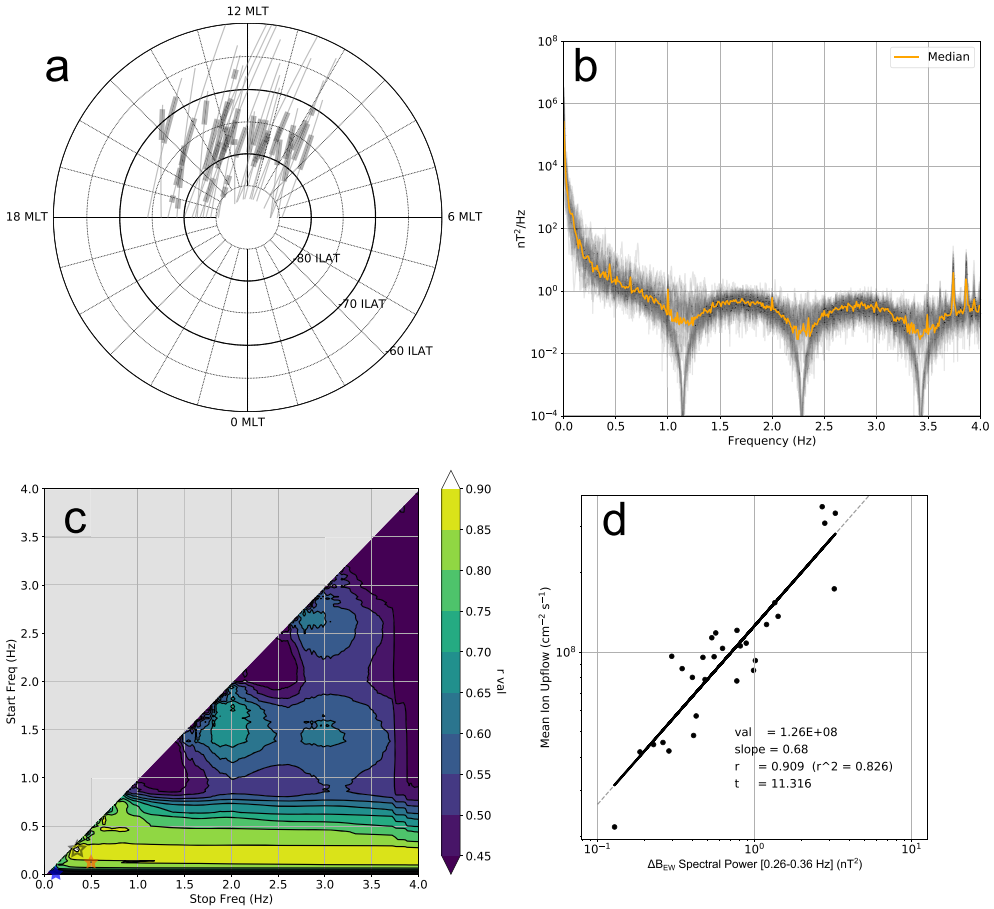

Figure 6. Ion and ΔB_{EW} statistics from 29 SH cusp region passes between 24 May and 5 June in 1998. The format of all panels is identical to corresponding panels in Figure 3. (a) Portions of orbits between −87° and −60° MLat, 6–18 MLT, and at or above 3,800-km altitude. Thick lines indicate identified ion outflow. In panel (d) the spacecraft frame frequency band that yields the highest correlation coefficient is 0.26–0.36 Hz.

3.3. Southern Hemisphere, January 1999 (Local Summer)

Figure 5 shows the results of analysis of 19,900 frequency bands between 0 and 4 Hz for 32 SH cusp region passes occurring between 8 and 15 January 1999, corresponding to local summer. The layout is identical to that of Figure 3. Figure 5a shows that ion outflows are mostly observed at MLat $\gtrsim 70°$ during these passes. The relatively small number of outflow observations made below these magnetic latitudes correspond to the portion of the 8-day observational period that coincides with a geomagnetic storm ($Dst_{\mathrm{min}} = -110$ nT) during 13–17 January.

Figure 5b shows that the individual PSD estimates (transparent black lines) and median PSD (orange line) are comparable to the PSD estimates and median PSD shown in Figure 3b. The median PSD ranges over ~7 orders of magnitude and decreases by more than 3 orders of magnitude between 0 and ~0.2 Hz. Similar to the artifacts visible in Figure 3b, the spiked spectral features at $\gtrsim$3.5 Hz are also artifacts related to the `ucla_mag_despin` routine. The troughs at ~1.25, 2.35, and 3.45 Hz are related to the recursive filter of the fluxgate magnetometer.

In Figure 5c, the correlation coefficient $r \geq 0.9$ for nearly 50% of all spacecraft frame frequency bands considered. Correlation coefficients $r \geq 0.90$ correspond to frequency bands given by either 1 Hz $\leq f_{\mathrm{bot}} \leq$ 1.6 Hz and $f_{\mathrm{bot}} \leq f_{\mathrm{top}} \leq 2.6$ Hz, or 0.1 Hz $\leq f_{\mathrm{bot}} \leq 0.6$ Hz and 0.2 Hz $\leq f_{\mathrm{top}} \leq 4$ Hz. In particular the spacecraft frame frequency band 1.6–1.74 Hz yields the highest correlation coefficient $r = 0.927$, with a best fit relationship $J_{\parallel,i} = 2.05 \times 10^9 P_{\mathrm{EW}}^{0.99}$.

3.4. Southern Hemisphere, May 1998 (Late Local Fall)

Figure 6 shows the results of analysis of 19,900 frequency bands between 0 and 4 Hz for 29 SH cusp region passes occurring between 24 May and 5 June 1999, corresponding to late fall. The layout is identical to that

of Figure 3. Figure 6a shows that ion outflows are mostly observed at MLat $\gtrsim 70°$ during these passes. The two regions of outflow over 14–15.5 MLT and near or below 70° MLat were observed during periods of weak geomagnetic activity ($Dst_{\min} = -34$ nT) that occurred intermittently during the 13-day observational period.

Figure 6b shows that the individual PSD estimates (transparent black lines) and median PSD (orange line) vary less overall than the PSD estimates shown in Figure 3b. The median PSD ranges over more than 6 orders of magnitude overall and decreases by more than 3 orders of magnitude over 0–0.2 Hz. The two spikes that reach ~10 nT^2/Hz at ~3.7 and 3.85 Hz are artifacts related to the `ucla_mag_despin` routine, whereas the deep troughs at ~1.2, 2.35, and 3.45 Hz are related to the recursive filter of the fluxgate magnetometer.

Figure 6c shows that the highest correlation coefficients ($r \geq 0.85$) correspond to spacecraft frame frequency bands such that 0.2 Hz $\leq f_{\text{bot}} \leq$ 0.4 Hz, 0.25 Hz $\leq f_{\text{top}} \leq$ 4 Hz. The frequency band 0.26–0.36 Hz yields the highest correlation coefficient $r = 0.909$, with a best fit relationship $J_{\parallel,i} = 1.26 \times 10^8 P_{\text{EW}}^{0.68}$.

4. Discussion and Summary

Two primary goals of this study are validation of the spectral method for studying the relationship between field fluctuations and upward ion fluxes, and expansion of the original data set considered by S05 and B11 to the Southern Hemisphere and other seasons. Results in Figures 2–6 demonstrate that empirical relationships very similar to those reported by S05 and B11 arise without inclusion of electric field measurements, and without recourse to visual determination of the cutoff energy (see sections 2.1 and 2.3). While we believe these aspects are significant, our methodology and data sets are nevertheless subject to their own limitations.

First, the algorithm for automated identification of ion outflows presented in section 2.1 is well suited to cusp region energetic ion outflows, but likely misses other forms of energetic ion up/outflows that are more typical at other local times, such as nightside ion beams (Kondo et al., 1990). We have elsewhere developed and employed an algorithm for automated identification of ion beams (Hatch, Chaston et al. 2018), which could be employed in possible future work dealing with the relationship between ion beams and field fluctuations.

Second, throughout this study we have relied on the assumption of S05 and B11 that the relationship between upward ion flux and field fluctuations is of the form of a power law. The scatter plots shown in the b panels of Figures 2–6 provide clear evidence that such a relationship could be derived from first principles for the presented ranges of spectral powers and outflow fluxes, but leave as an open question whether a power law relationship is valid for fluxes and spectral powers outside the observed ranges. Existing attempts in the literature (Horwitz & Zeng, 2009; Moore & Khazanov, 2010; Varney et al., 2016) to theoretically reproduce the observations presented by S05 and B11 represent important steps toward a full theoretical description, but each study points to a need for more observational data.

Third, regarding field measurements, we have not used FAST electric field measurements to estimate the field-aligned Poynting flux, as did S05 and B11. Two disadvantages of this approach, noted in section 2.3, are that it does not provide information about input electromagnetic energy, nor does it allow for inference of the relevant processes on the basis of techniques involving analysis of the perturbation electric and magnetic field ratio or plasma density perturbations (e.g., Wahlund et al., 1998; Figure A1 in S05). On the other hand this approach opens the exploitation of magnetic field measurements as a possibly powerful alternative to Poynting flux measurements in studies of energetic ion outflows, and could yield a significant contribution to filling the knowledge gaps mentioned in section 1. This approach is the planned subject of future work.

Fourth, we have exclusively considered the east-west component of the measured magnetic field. This component yields overall higher correlation coefficients than those yielded when we instead use the north-south component of the measured magnetic field, though in many cases the differences are slight. Our choice is also motivated by the preferential east-west orientation of Alfvénic magnetic field perturbations, as already discussed in section 1.

Fifth, the dayside cusp region is the site of small-scale, relatively large amplitude field-aligned currents (Kervalishvili & Lühr, 2013; Neubert & Christiansen, 2003; Rother et al., 2007; Watermann et al., 2009). As an alternative to calculating the correlation coefficient between $\langle J_{\parallel,\text{up}} \rangle$ and ΔB_{EW} spectral power P_{EW}, as we have done here, we could have correlated $\langle J_{\parallel,\text{up}} \rangle$ with estimates of field-aligned current amplitude. This latter type of correlation study between field-aligned current amplitude and various ionospheric and thermospheric parameters has in fact been carried out elsewhere (Kervalishvili & Lühr, 2013; Shen et al., 2016).

Table 2
Statistics of r Correlation coefficient in panel c of Figures 3–6

Group	Section	Time period	Hemisphere	r_{median}	r_{mean}	r_{spread} $r_{0.75} - r_{0.25}$ [a]
1	3.1	September 1998	Northern	0.722	0.732	0.173
2	3.2	December 1996	Northern	0.536	0.491	0.416
3	3.3	January 1999	Southern	0.899	0.871	0.049
4	3.4	May 1998	Southern	0.569	0.601	0.239

[a]The $r_{0.25}$ and $r_{0.75}$ are respectively the first and third quartiles of the distribution of r values.

We have opted not to perform this type of analysis, primarily because our study takes the work of S05 and B11 as starting points of reference. Neither of these studies dealt with field-aligned current estimates. Performing a correlation study with the data sets we have presented that is based on field-aligned currents could yield additional physical insight, but we deem such work outside the scope of the present study.

We believe that a critical aspect of this study is the stringent criteria on spacecraft MLT, Mlat, altitude, and direction of approach to the cusp region. We have discussed in section 2 that the purpose of these criteria is to reduce potential Doppler shifting of field measurements and to exclude ram ions as much as possible. With these criteria there emerges from the analysis of each group of orbits some common characteristics of the relationship between ion outflows and east-west magnetic field fluctuations, which we now discuss. (Text S1 and Figures S1–S4 in the supporting information provides versions of the analysis in Figures 3–6 with the restriction to altitudes of 3,800 km or greater relaxed).

The most salient feature in panel c for each of Figures 3–6 in section 3 is that the correlation between ion outflows and east-west magnetic field fluctuations ΔB_{EW} is high for spacecraft frame frequencies $f_{sc} \lesssim 0.7$ Hz in every case. Only orbits in Group 2 (section 3.2) involve pole-to-equator traversals of the cusp region, and as we discuss below in connection with Table 4, Doppler shifting of Group 2 spacecraft frame frequency bands is one possible explanation for the different frequency characteristics of Group 2 orbits relative to the three groups of orbits, for which FAST approaches the cusp region from the equator. For Groups 1 and 4 orbits the upper limit of frequencies corresponding to high correlations is even narrower, $f_{sc} \lesssim 0.4$ Hz.

On the other hand, the frequency characteristic of Group 3 orbits in Figure 5c are distinct from the frequency characteristics of the other three groups: the overall distribution of r values for Group 3 orbits is overall significantly shifted to higher r values, and is spread over an overall smaller range. Table 2 summarizes the properties of the distribution of r values for each of the four groups of orbits. From Table 2 it is evident that both the median and mean r values for Group 3 orbits are much higher than the median and mean r values for any of the other three groups of orbits. In other words, for Group 3 orbits the correlation coefficient between $\langle J_{\parallel,\mathrm{up}} \rangle$ and P_{EW} is high almost regardless of frequency band.

Regardless of the direction of approach or the distribution of r values, panel c for each of Figures 3–6 shows that the correlation coefficient r varies primarily with the lower bound f_{bot} (y axis) of a given frequency band, while the dependence on the upper bound f_{top} (x axis) is relatively much weaker. The dominating role of f_{bot} in the variation of the correlation coefficient arises due to the general shape of the PSD estimates corresponding to each orbit (transparent black lines in panel b for each of Figures 3–6). Each PSD estimate exhibits a logarithmic, and approximately monotonic, decrease with increasing frequency up to $f_{sc} \sim 1$ Hz. Thus, the spectral power P_{EW} obtained from integration of any frequency band with a lower bound $f_{bot} \leq 1$ Hz is primarily determined by f_{bot} and largely invariant with respect to the upper bound f_{top}.

To make the results shown in Figures 3–6 easily implementable for modelers, Table 3 provides best fit relationships of the form $J_{\parallel,i} = J_{0,i} P_{\mathrm{EW}}^{\gamma}$ between upward ion flux mapped to 130-km altitude $J_{\parallel,i}$, spectral power P_{EW}, and power law index $\gamma \simeq 0.7$–1.2 for the spacecraft frame frequency band 0.18–1.46 Hz. We have chosen this frequency band because it yields the "maximum average correlation coefficient" $\bar{r}_{\mathrm{max}}$ obtained as follows.

Let $r_i(f_{\mathrm{bot}}, f_{\mathrm{top}})$ be the correlation coefficient for the ith orbit group, where $i \in (0, 1, 2, 3)$ indicates one of the four groups of orbits in Tables 1 and 3, and $(f_{\mathrm{bot}}, f_{\mathrm{top}})$ denotes any of the 19,900 frequency bands represented by the x and y axes of panel c in Figures 3–6. Then the "maximum average correlation coefficient" $\bar{r}_{\mathrm{max}} =$

Table 3
Best Fit Relationships for the Frequency Band 0.18–1.46 Hz

Group	Section	Time period	Hemisphere	$J_{\|\|,i} = J_{0,i} P_{\mathrm{EW}}^{\gamma}$ $(J_{0,i}, \gamma)^{\mathrm{b}}$	r	$\langle F10.7 \rangle_{27}{}^{\mathrm{a}}$ $10^{-22}\mathrm{J/m^2}$
1	3.1	September 1998	Northern	$(10^{7.001}, 1.168)$	0.924	144–146
2	3.2	December 1996	Northern	$(10^{7.730}, 0.708)$	0.745	75–76
3	3.3	January 1999	Southern	$(10^{7.412}, 0.981)$	0.919	137–143
4	3.4	May 1998	Southern	$(10^{7.598}, 0.784)$	0.882	105–111

[a] $J_{0,i}$ is the mapped upward ion flux (in $\mathrm{cm^{-2}\ s^{-1}}$) for nominal spectral power $P_{\mathrm{EW}} = 1\ \mathrm{nT^2}$. P_{EW} is the integral of the ΔB_{EW} PSD (in $\mathrm{nT^2/Hz}$) over 0.18–1.46 Hz. [b] The angle brackets $\langle\rangle_{27}$ denote a backward-looking average over a 27-day window.

$\max(r_A) = \max(\frac{1}{4}\sum_i r_i(f_{\mathrm{bot}}, f_{\mathrm{top}})) = 0.868$ is obtained for the frequency band ($f_{\mathrm{bot}} = 0.18$ Hz, $f_{\mathrm{top}} = 1.46$ Hz). This frequency band also yields the maximum if we instead calculate the maximum via the geometric mean or the harmonic mean.

Figure 7a shows, for all 132 orbits used in this study, individually observed ion outflow fluxes (mapped to 130-km altitude) as a function of season. Groups 1 and 3 upward ion fluxes (red plus and blue x symbols), which respectively occurred near fall equinox and summer solstice, are overall greater than Groups 2 and 4 upward ion fluxes (purple circle and orange triangle symbols), which both occurred near winter solstice. This observation leads us to consider the dependence of upward ion fluxes on season.

Two causes of long-term variation in the properties of outflowing ions are season and solar cycle. On point of season, Yau et al. (1985) found that the occurrence of O^+ upflows over altitudes of 8,000 to 23,000 km is favored by summer solstice, while they found no significant variation of the occurrence of H^+ with season. On point of solar cycle, Yau et al. (1988) found that the outflowing O^+/H^+ ratio increases by an order of magnitude from solar minimum to solar maximum.

Group 1 orbits (23–26 September 1998) occurred near fall equinox during which 27-day-averaged F10.7 indices $\langle F_{10.7} \rangle_{27}$ = 144–146, the highest F10.7 range for all four orbit groups (rightmost column in Table 3; F10.7 values were obtained from https://omniweb.gsfc.nasa.gov/form/dx1.html). Group 2 orbits (30 December 1996 to 7 January 1997) occurred near local winter, during which $\langle F_{10.7} \rangle_{27} = 75$–76 (i.e., near solar minimum), the lowest range of $\langle F_{10.7} \rangle_{27}$ values for all four orbit groups. Based on the higher range of

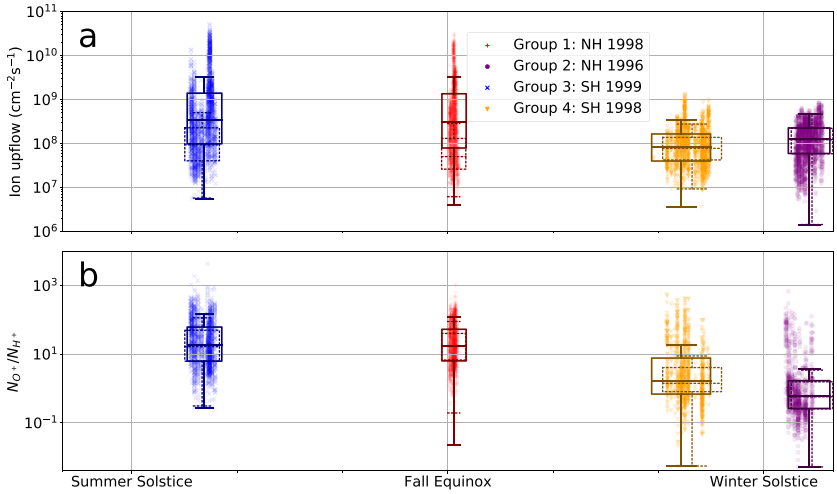

Figure 7. (a) Scatterplots of observed upward ion fluxes for each of the four groups of orbits analyzed in section 3 and indicated in Tables 1–4, as a function of season. (b) O^+/H^+ density ratios derived from TEAMS mass spectrometer measurements for 114 of the 132 orbits shown in panel a (see text). In both panels a solid-line box plot is shown for each orbit group to indicate the median as well as upper and lower quartiles Q3 and Q1. The top and bottom lines for each box plot respectively indicate the values Q3 + 1.5IQR and Q1 − 1.5IQR, with IQR ≡ Q3 − Q1. A dashed-line boxplot provides the same statistics for geomagnetically quiet periods ($K_p \leq 2.5$).

$\langle F_{10.7}\rangle_{27}$ values observed during Group 1 orbits, we expect that Group 1 outflows are relatively much richer in O^+ than Group 2 outflows.

Group 3 orbits (8–15 January 1999) occurred near summer solstice with $\langle F_{10.7}\rangle_{27}$ = 137–143, only slightly lower than the Orbit Group 1 $\langle F_{10.7}\rangle_{27}$ range. Group 4 orbits (24 May to 5 June 1998) occurred near winter solstice with $\langle F_{10.7}\rangle_{27}$ = 105–111, intermediate to the $\langle F_{10.7}\rangle_{27}$ ranges for the other three orbit groups.

Based on these differences in season and solar cycle for the four groups of orbits, we expect that Groups 1 and 3 outflows are richest in O^+, with Group 4 outflows somewhat poorer and Group 2 outflows poorest in O^+. To directly demonstrate the existence of these differences, Figure 7b shows the O^+/H^+ density ratio derived from analysis of ion composition measurements made by the Time-of-Flight Energy, Angle, Mass Spectrograph (TEAMS) instrument (Klumpar et al., 2001) aboard FAST. As with upward ion fluxes in panel a, each data point represents an individual O^+/H^+ density ratio estimate for TEAMS observations made during 114 of the 132 orbits shown in Figure 7a. (TEAMS measurements were unavailable for the other 18 passes.) The density moment is calculated for each species distribution function measured by TEAMS by integrating over all angles, and from 4 eV up to the IESA energy cutoff E_{top} given by the outflow identification algorithm in section 2.1. (For example, E_{top} is indicated by the pink line in Figure 1d.) Each TEAMS measurement is required to meet the same criteria from section 2 that we have applied to FAST IESA and magnetometer data, and we include only those TEAMS measurements that correspond to time periods when ion outflow is positively identified in IESA measurements.

As mentioned in section 3, moderate to high levels of geomagnetic activity were also observed during Groups 1, 3, and 4 orbits. To exclude the effects of geomagnetic activity, the boxplots composed of dashed lines in Figures 7a and 7b indicate outflow and O^+/H^+ statistics for $K_p \leq 2.5$. (K_p values were obtained from the publicly available OMNI database at https://omniweb.gsfc.nasa.gov/form/dx1.html.)

Both sets of boxplots in Figure 7b indicate that the upflows observed near or during summer solstice are relatively much richer in O^+ than those during winter, as expected. On the other hand, comparison of the dashed-line boxplots reveals that the overall distributions of "geomagnetic quiescence" outflow fluxes are mostly similar and apparently somewhat independent of season. This fact highlights that geomagnetic activity and seasonal effects may be conflated in the analysis presented in Figures 3–6.

Removing outflowing ion fluxes observed during $K_p > 2.5$ unfortunately removes more than 50% of all observations in Groups 1 and 3 orbits. We therefore have insufficient statistics to perform a separate analysis based only on observations during geomagnetic quiescence, and in this study we are not able to untangle the effects geomagnetic activity and seasonal variations.

TEAMS measurements are currently undergoing additional calibration and dead-time correction by a study coauthor (E. J. Lund). At present these measurements likely underestimate the actual densities of each species and are not suitable for the correlation analysis that we have performed in section 3. But the overall trends and order-of-magnitude differences are sufficient to underscore that the composition of ionospheric outflow likely play a role in seasonal variations of the relationship between ionospheric outflow and magnetic field perturbations that we have demonstrated. Thus Figure 7 demonstrates that ion composition should not be neglected in any comprehensive model of wave-driven energetic ion outflows. Although outside the scope of this study, we reserve extended treatment of ion composition as a possible focus of future work.

On the question of Doppler shifting raised in section 2 and at the beginning of this section, other studies based on FAST and Freja observations (Chaston et al., 2006; Stasiewicz et al., 2000) have explicitly demonstrated that low-frequency waves with short perpendicular wavelengths (of order ~0.01–10 km) on the dayside are observed by these satellites as broadband waves in the spacecraft frame of reference via Doppler shift.

While we emphasize that our approach does not allow us to determine the properties of the field perturbations we have analyzed in this study, we show here that the two following assumptions

1. magnetic field perturbations observed by FAST over 0–4 Hz in the spacecraft frame of reference are either spatial structures or wave structures with frequencies near zero (i.e., $\omega(\mathbf{k}) \simeq 0$);
2. the variation of magnetic field perturbations is primarily perpendicular to the background magnetic field (i.e., $k_\perp \gg k_\parallel$);

Table 4
Estimated Transverse Spatial Scales $L_\perp$ Corresponding to Ion Outflow[a]

Group	Section	Time period	Hemisphere	$r_{90\%}$[b]	f_{bot} range[c] (Hz)	$\lvert v_{F,\perp} - V \rvert$ (km/s)	$L_\perp$[d] (km)
1	3.1	September 1998	Northern	0.91	0.04–0.26	4.5	17–110
2	3.2	December 1996	Northern	0.74	0.15–0.64	6.5	10–42
3	3.3	January 1999	Southern	0.91	0.13–0.28	4.5	16–35
4	3.4	May 1998	Southern	0.83	0.09–0.34	4.5	13–49

[a]Via equation 3, which assumes observed B field perturbations have an intrinsic frequency near zero. [b]For each orbit group, the lower bound of the highest 10% of all calculated r values. [c]Approximate range of "start frequencies" f_{bot} for which correlation coefficient $r \geq r_{90\%}$. [d]Perpendicular scale size near FAST apogee at ~4,100-km altitude.

appear consistent with the results shown in panel c of Figures 3–6.

With these assumptions the observed spacecraft frame frequencies arise via Doppler shifting according to

$$\omega_{sc}(\mathbf{k}) = 2\pi f_{sc}(\mathbf{k}) = |\mathbf{k} \cdot (\mathbf{v}_F - \mathbf{V})| \approx |k_\perp (v_{F,\perp} - V)|, \quad (2)$$

where $v_{F,\perp}$ is the perpendicular speed of FAST and V is the poleward plasma convection speed. Thus, the spacecraft frame frequency f_{sc} corresponds to a perpendicular spatial scale

$$L_\perp = \frac{|v_{F,\perp} - V|}{f_{sc}}. \quad (3)$$

Typical convection speeds in the dayside cusp region at ionospheric altitudes (i.e., hundreds of kilometers) range from hundreds of m/s up to 2–3 km/s during active conditions (Moen et al., 1996; Skjæveland et al., 2011, 2014), and typical speeds of FAST perpendicular to the background magnetic field near apogee are $|v_{F,\perp}|$ =5.2–5.6 km/s.

We assume V =1 km/s and $v_{F,\perp} = \pm 5.5$ km/s, where the positive sign corresponds to poleward orbits (i.e., Groups 1, 3, and 4) and the negative sign corresponds to equatorward orbits (i.e., Group 2). We then apply equation 3 to the range of "start frequencies" f_{bot}, indicated on the y axis of panel c for Figures 3–6, for which $r \geq r_{90\%}$. (The subscript "0.9" denotes the 0.9 quantile of all calculated r values for a particular orbit group. For example, 10% of all r values in Figure 3c are 0.91 or greater; thus $r_{90\%} = 0.91$ in Table 4.)

The rightmost column of Table 4 shows the resulting range of perpendicular spatial scales near FAST apogee for each group of orbits. If the above-stated assumptions are valid, east-west field perturbations with perpendicular spatial scales of order tens of kilometers are associated with ion outflow. Indeed, it has been shown (e.g., Stasiewicz et al., 2000 and section 2.2 as well as Figure 3 of Chaston et al., 2007) that much of the temporal variation observed in the FAST and Freja spacecraft frame of references at these altitudes is due to Doppler shifting of dispersive Alfvén wave structures.

As a consistency check, applying equation (2) to the range of scale sizes $L_\perp$ = 10–42 km corresponding to Group 2 in Table 4 shows that if FAST had been moving poleward instead of equatorward in the presence of plasma convecting poleward at 1 km/s, these scale sizes would have been observed over the spacecraft frequency range f_{bot} = 0.11–0.44 Hz. Though not proof, range is more consistent with the f_{bot} ranges for Groups 1, 3, and 4 in Table 4, and suggests that the above assumptions are at least plausible.

These perpendicular scales are in between large scales (of order hundreds or thousands of kilometers, corresponding to quasi-static field-aligned currents and the electrojets) and kinetic scales (of order 1 m to a few km, corresponding to local ion gyroradii and the electron inertial length) within and in the vicinity of the dayside cusp. Thus, instead of corresponding to direct driving of energetic ion outflow, these scales may be related to a number of processes that are associated with ion outflow.

Both simulations (Chaston et al., 2004; Génot et al., 2004; Rankin et al., 2005) and satellite observations (Chaston et al., 2006) have shown that the interaction of shear Alfvén waves with a preexisting ionospheric density irregularity produces field-aligned broadband electron precipitation, transverse ion acceleration, ion heating, and plasma depletion (Chaston et al., 2006, Figure 6). This interaction also leads to phase

mixing and the production of field fluctuations over perpendicular scales ranging from the scale size of the density irregularity down to and below the electron inertial length, typically of order km in the magnetosphere-ionosphere transition region.

As observed by Lotko and Zhang (2018), evidence that these perpendicular spatial scales are associated with Alfvén waves has been reported by Ishii et al. (1992). Using DE-2 measurements at 300-km altitude they showed that field perturbations over DE-2 spacecraft frame frequencies of $\gtrsim$0.25 Hz were more consistent with an Alfvénic rather than a quasi-static interpretation; treating this frequency range as resulting from Doppler-shifted structures, they reported perpendicular spatial scales of $\lesssim$30 km at 300-km altitude ($\lesssim$60 km near FAST apogee).

As an additional plausibility check, we have determined from the Hatch et al. (2017) inertial Alfvén wave database that inertial Alfvén waves are observed during 83% (109 out of 132 total) of the cusp region passes. This percentage is presented only for the purpose of indicating that Alfvén waves are in fact often present during observed upflows, with a median of 26 Alfvénic current filaments identified per orbit for all 132 orbits.

Here we have favored interpretation of observed dayside field perturbations at FAST altitudes as Doppler-shifted Alfvénic structures. We should emphasize that this interpretation, while plausible, is not the only possibility. At mHz- to Hz-range frequencies, there exist alternative interpretations based on ion-cyclotron waves, ion-acoustic waves, and field gradients or energy density inhomogeneities (André et al., 1990, 1998; Bouhram et al., 2002; Chernyshov et al., 2017; Chugunin et al., 2018; Kintner et al., 2000; Seyler & Wahlund, 1996; Wahlund et al., 1998). Our methodology does not allow for positive identification or exclusion of any of these alternative processes.

In conclusion, in this study we have validated and applied a new methodology for examining the relationship between ion outflows and field fluctuations in the dayside cusp region in both hemispheres and as a function of season. We have presented an algorithm that achieves automated identification of ionospheric-origin ion outflows, and a spectral method for analysis of the relationship between these outflows and east-west magnetic field perturbations over nearly arbitrary frequency bands. Using four groups of orbits, two from each hemisphere, we have found that field perturbations over spacecraft frame frequencies of less than 0.7 Hz show the highest correlation with cusp region ion outflows. Best fit relationships between these field perturbations and ion outflows yield power law indices between 0.7 and 1.2, where the lowest power law values are associated with winter/late fall and the highest values associated with fall equinox/summer.

Previous studies indicate that magnetic field perturbations over these frequency ranges are associated with a variety of wave modes. We have not attempted to positively determine or exclude which wave modes are in operation during the reported observations, although we have outlined the plausibility of an interpretation based on Alfvén waves. Regardless of wave mode we have shown that if the observed perturbations are related to purely Doppler-shifted structures, they correspond to perpendicular scale sizes of several to tens of kilometers.

We have also demonstrated that ion composition likely plays a significant role in the relationship between ionospheric-origin energetic outflows and field fluctuations. This study underscores the need for much larger ion outflow data sets made up of observations for which the effects of ram ions and Doppler shifting due to spacecraft motion are consistently accounted for or otherwise mitigated.

Acknowledgments
Observations and measurements made by the FAST spacecraft are publicly available as a Level 1 data product via SDT ("Science Data Tool"), downloadable via http://sprg.ssl.berkeley.edu/~sdt/SdtReleases.html, or via NASA/GSFC Space Physics Data Facility's Coordinated Data Analysis Web (CDAWeb; https://cdaweb.sci.gsfc.nasa.gov/index.html/). Work at the Birkeland Center for Space Science and the University of Bergen was funded by the Research Council of Norway/CoE under Contract 223252/F50 and by ESA Contract 4000126731 in the framework of EO Science for Society. Work at the University of New Hampshire is supported by the National Science Foundation under Grant 1502937. S. M. Hatch thanks J. Bonnell, M. Burleigh, C. Chaston, and A. Yau for helpful commentary and feedback on the draft manuscript of this study.

References

André, M., Norqvist, P., Andersson, L., Eliasson, L., Eriksson, A. I., Blomberg, L., et al. (1998). Ion energization mechanisms at 1700 km in the auroral region. *Journal of Geophysical Research*, *103*(A3), 4199–4222. https://doi.org/10.1029/97JA00855

André, M., & Yau, A. (1997). Theories and observations of ion energization and outflow in the high latitude magnetosphere. *Space Science Reviews*, *80*(1), 27–48. https://doi.org/10.1023/A:1004921619885

André, M., Crew, G. B., Peterson, W. K., Persoon, A. M., Pollock, C. J., & Engebretson, M. J. (1990). Ion heating by broadband low-frequency waves in the cusp/cleft. *Journal of Geophysical Research*, *95*(A12), 20,809–20,823. https://doi.org/10.1029/JA095iA12p20809

Bouhram, M., Dubouloz, N., Malingre, M., Jasperse, J. R., Pottelette, R., Senior, C., et al. (2002). Ion outflow and associated perpendicular heating in the cusp observed by Interball Auroral Probe and Fast Auroral Snapshot. *Journal of Geophysical Research*, *107*(A2), 1023. https://doi.org/10.1029/2001JA000091

Bouhram, M., Klecker, B., Miyake, W., Rème, H., Sauvaud, J.-A., Malingre, M., et al. (2004). On the altitude dependence of transversely heated O+ distributions in the cusp/cleft. *Annales Geophysicae*, *22*(5), 1787–1798. https://doi.org/10.1029/2001JA000091

Brambles, O. J., Lotko, W., Damiano, P. A., Zhang, B., Wiltberger, M., & Lyon, J. (2010). Effects of causally driven cusp O+ outflow on the storm time magnetosphere-ionosphere system using a multifluid global simulation. *Journal of Geophysical Research*, *115*, A00J04. https://doi.org/10.1029/2010JA015469

Brambles, O. J., Lotko, W., Zhang, B., Wiltberger, M., Lyon, J., & Strangeway, R. J. (2011). Magnetosphere sawtooth oscillations induced by ionospheric outflow. *Science*, *332*(6034), 1183–1186.

Burchill, J. K., Knudsen, D. J., Clemmons, J. H., Oksavik, K., Pfaff, R. F., Steigies, C. T., et al. (2010). Thermal ion upflow in the cusp ionosphere and its dependence on soft electron energy flux. *Journal of Geophysical Research*, *115*, A05206. https://doi.org/10.1029/2009JA015006

Carlson, C. W., Mcfadden, J. P., Turin, P., Curtis, D. W., & Magoncelli, A. (2001). The electron and ion plasma experiment for FAST. *Space Science Reviews*, *98*(1), 33–66. https://doi.org/10.1023/A:1013139910140

Chaston, C. C., Bonnell, J. W., Carlson, C. W., McFadden, J. P., Ergun, R. E., & Strangeway, R. J. (2003). Properties of small-scale Alfvén waves and accelerated electrons from FAST. *Journal of Geophysical Research*, *108*(A4), 8003. https://doi.org/10.1029/2002JA009420

Chaston, C. C., Bonnell, J. W., Carlson, C. W., Mcfadden, J. P., Ergun, R. E., Strangeway, R. J., & Lund, E. J. (2004). Auroral ion acceleration in dispersive Alfven waves. *Journal of Geophysical Research*, *109*, A04205. https://doi.org/10.1029/2003JA010053

Chaston, C. C., Carlson, C. W., McFadden, J. P., Ergun, R. E., & Strangeway, R. J. (2007). How important are dispersive Alfvén waves for auroral particle acceleration? *Geophysical Research Letters*, *34*, L07101. https://doi.org/10.1029/2006GL029144

Chaston, C. C., Genot, V., Bonnell, J. W., Carlson, C. W., McFadden, J. P., Ergun, R. E., et al. (2006). Ionospheric erosion by Alfvén waves. *Journal of Geophysical Research*, *111*, A03206. https://doi.org/10.1029/2005JA011367

Chaston, C. C., Hull, A. J., Bonnell, J. W., Carlson, C. W., Ergun, R. E., Strangeway, R. J., & McFadden, J. P. (2007). Large parallel electric fields, currents, and density cavities in dispersive Alfvén waves above the aurora. *Journal of Geophysical Research*, *112*, A05215. https://doi.org/10.1029/2006JA012007

Chernyshov, A. A., Ilyasov, A. A., Mogilevsky, M. M., Golovchanskaya, I. V., & Kozelov, B. V. (2017). Excitation of ion-acoustic waves in the high-latitude ionosphere. *Geomagnetism and Aeronomy*, *57*(3), 308–316. https://doi.org/10.1134/S0016793217030045

Chugunin, D. V., Klimenko, M. V., Chernyshov, A. A., Klimenko, V. V., Il'yasov, A. A., & Luk'yanova, R. Y. (2018). Heating of ions by small-scale electric field inhomogeneities in the auroral ionosphere during geomagnetic disturbances. *Geomagnetism and Aeronomy*, *58*(1), 50–61. https://doi.org/10.1134/S001679321801005X

Elphic, R. C., Means, J. D., Snare, R. C., Strangeway, R. J., Kepko, L., & Ergun, R. E. (2001). Magnetic field instruments for the Fast Auroral Snapshot explorer. *Space Science Reviews*, *98*, 151–168.

Ergun, R. E., Carlson, C. W., Mozer, F. S., Delory, G. T., Temerin, M., Mcfadden, J. P., et al. (2001). The Fast Satellite Fields instrument. *Space Science Reviews*, *98*(1-2), 67–91.

Fernandes, P. A., Lynch, K. A., Zettergren, M., Hampton, D. L., Bekkeng, T. A., Cohen, I. J., et al. (2016). Measuring the seeds of ion outflow: Auroral sounding rocket observations of low-altitude ion heating and circulation. *Journal of Geophysical Research: Space Physics*, *121*, 1587–1607. https://doi.org/10.1002/2015JA021536

Génot, V., Louarn, P., & Mottez, F. (2004). Alfvén wave interaction with inhomogeneous plasmas: acceleration and energy cascade towards small-scales. *Annales Geophysicae*, *22*(6), 2081–2096.

Hatch, S. M., Chaston, C. C., & LaBelle, J. (2018). Nonthermal limit of monoenergetic precipitation in the auroral acceleration region. *Geophysical Research Letters*, *45*, 10,167–10,176. https://doi.org/10.1029/2018GL078948

Hatch, S. M., & LaBelle, J. (2018). Application of a new method for calculation of low-frequency wave vectors. In G. Fischer, G. Mann, M. Panchenko, & P. Zarka (Eds.), *Planetary radio emissions viii* (pp. 247–260). Vienna: Austrian Academy of Sciences Press.

Hatch, S. M., Labelle, J., Lotko, W., Chaston, C. C., & Zhang, B. (2017). IMF control of Alfvénic energy transport and deposition at high latitudes. *Journal of Geophysical Research: Space Physics*, *122*, 12,189–12,211. https://doi.org/10.1002/2017JA024175

Heelis, R. A., & Hanson, W. B. (1998). *Measurements of thermal ion drift velocity and temperature using planar sensors*, Geophysical Monograph Series. https://doi.org/10.1029/GM102p0061

Horwitz, J. L., & Zeng, W. (2009). Physics-based formula representations of high-latitude ionospheric outflows: H^+ and O^+ densities, flow velocities, and temperatures versus soft electron precipitation, wave-driven transverse heating, and solar zenith angle effects. *Journal of Geophysical Research*, *114*, A01308. https://doi.org/10.1029/2008JA013595

Howarth, A., & Yau, A. W. (2008). The effects of IMF and convection on thermal ion outflow in magnetosphere-ionosphere coupling. *Journal of Atmospheric and Solar-Terrestrial Physics*, *70*(17), 2132–2143.

Ishii, M., Sugiura, M., Iyemori, T., & Slavin, J. A. (1992). Correlation between magnetic and electric field perturbations in the field-aligned current regions deduced from DE 2 observations. *Journal of Geophysical Research*, *97*(A9), 13,877–13,887. https://doi.org/10.1029/92JA00110

Kervalishvili, G. N., & Lühr, H. (2013). The relationship of thermospheric density anomaly with electron temperature, small-scale FAC, and ion up-flow in the cusp region, as observed by CHAMP and DMSP satellites. *Annales Geophysicae*, *31*(3), 541–554.

Kintner, P. M., Franz, J., Schuck, P., & Klatt, E. (2000). Interferometric coherency determination of wavelength or what are broadband ELF waves? *Journal of Geophysical Research*, *105*(A9), 21,237–21,250. https://doi.org/10.1029/1999JA000323

Klumpar, D. M., Möbius, E, Kistler, LM, Popecki, M., Hertzberg, E., Crocker, K., et al. (2001). The Time-of-Flight Energy, Angle, Mass Spectrograph (TEAMS) experiment for FAST. *Space Science Reviews*, *98*(1), 197–219. https://doi.org/10.1023/A:1013127607414

Kondo, T., Whalen, B. A., Yau, A. W., & Peterson, W. K. (1990). Statistical analysis of upflowing ion beam and conic distributions at DE 1 altitudes. *Journal of Geophysical Research*, *95*(A8), 12,091–12,102. https://doi.org/10.1029/JA095iA08p12091

Kronberg, E. A., Iannis, M. A.-A., Delcourt, D. C., Grigorenko, E. E., Kistler, L. M., Kuzichev, I. V., et al. (2014). Circulation of heavy ions and their dynamical effects in the magnetosphere: Recent observations and models. *Space Science Reviews*, *184*, 173–235.

Laundal, K. M., & Richmond, A. D. (2016). Magnetic coordinate systems. *Space Science Reviews*, *1-4*, 27–59. https://doi.org/10.1007/s11214-016-0275-y

Lee, S. H., Zhang, H., Zong, Q.-G., Otto, A., Rème, H., & Liebert, E. (2016). A statistical study of plasmaspheric plumes and ionospheric outflows observed at the dayside magnetopause. *Journal of Geophysical Research: Space Physics*, *121*, 492–506. https://doi.org/10.1002/2015JA021540

Lotko, W., & Zhang, B. (2018). Alfvénic heating in the cusp ionosphere-thermosphere. *Journal of Geophysical Research: Space Physics*, *123*, 10,368–10,383. https://doi.org/10.1029/2018JA025990

Moen, J., Lockwood, M., Sandholt, P. E., Løvhaug, U. P., Denig, W. F., van Eyken, A. P., & Egeland, A. (1996). Variability of dayside high latitude convection associated with a sequence of auroral transients. *Journal of Atmospheric and Terrestrial Physics*, *58*(1), 85–96.

Moore, T. E., Fok, M.-C., Delcourt, D. C., Slinker, S. P., & Fedder, J. A. (2007). Global aspects of solar wind–ionosphere interactions. *Journal of Atmospheric and Solar-Terrestrial Physics*, *69*(3), 265–278.

Moore, T. E., & Horwitz, J. L. (2007). Stellar ablation of planetary atmospheres. *Reviews of Geophysics*, *45*, RG3002. https://doi.org/10.1029/2005RG000194

Moore, T. E., & Khazanov, G. V. (2010). Mechanisms of ionospheric mass escape. *Journal of Geophysical Research*, *115*, A00J13. https://doi.org/10.1029/2009JA014905

Moore, T. E., Pollock, C. J., & Young, D. T. (1998). Kinetic core plasma diagnostics, *Measurement techniques in space plasmas: Particles* (pp. 105–123). Washington, DC: American Geophysical Union. https://doi.org/10.1029/GM102p0105

Neubert, T., & Christiansen, F. (2003). Small-scale, field-aligned currents at the top-side ionosphere. *Geophysical Research Letters*, *30*(19), 2010. https://doi.org/10.1029/2003GL017808

Nilsson, H. (2011). Heavy ion energization, transport, and loss in the Earth's magnetosphere. In W. Liu & M. Fujimoto (Eds.), *The dynamic magnetosphere* (pp. 315–327). Dordrecht: Springer Netherlands.

Nilsson, H., Waara, M., Arvelius, S., Marghitu, O., Bouhram, M., Hobara, Y., et al. (2006). Characteristics of high altitude oxygen ion energization and outflow as observed by Cluster: a statistical study. *Annales Geophysicae*, *24*, 1099–1112.

Norqvist, P., André, M., & Tyrland, M. (1998). A statistical study of ion energization mechanisms in the auroral region. *Journal of Geophysical Research*, *103*(A10), 23,459–23,473. https://doi.org/10.1029/98JA02076

Peterson, W. K., Andersson, L., Callahan, B., Elkington, S. R., Winglee, R. W., Scudder, J. D., & Collin, H. L. (2008). Geomagnetic activity dependence of O^+ in transit from the ionosphere. *Journal of Atmospheric and Solar-Terrestrial Physics*, *71*(16), 1623–1629.

Rankin, R., Marchand, R., Lu, J. Y., Kabin, K., & Tikhonchuk, V. T. (2005). Theory of dispersive shear Alfvén wave focusing in Earth's magnetosphere. *Geophysical Research Letters*, *32*, L05102. https://doi.org/10.1029/2004GL021831

Richmond, A. D. (1995). Ionospheric electrodynamics using magnetic apex coordinates. *Journal of Geomagnetism and Geoelectricity*, *47*(2), 191–212.

Rother, M., Schlegel, K., & Lühr, H (2007). CHAMP observation of intense kilometer-scale field-aligned currents, evidence for an ionospheric Alfvén resonator. *Annales Geophysicae*, *25*(7), 1603–1615.

Seyler, C. E., & Wahlund, J.-E. (1996). Theory of nearly perpendicular electrostatic plasma waves and comparison to Freja satellite observations. *Journal of Geophysical Research*, *101*(A10), 21,795–21,813. https://doi.org/10.1029/96JA02041

Shen, Y., Knudsen, D. J., Burchill, J. K., Howarth, A., Yau, A., Redmon, R. J., et al. (2016). Strong ambipolar-driven ion upflow within the cleft ion fountain during low geomagnetic activity. *Journal of Geophysical Research: Space Physics*, *121*, 6950–6969. https://doi.org/10.1002/2016JA022532

Skjæveland, Å., Moen, J., & Carlson, H. C. (2011). On the relationship between flux transfer events, temperature enhancements, and ion upflow events in the cusp ionosphere. *Journal of Geophysical Research*, *116*, A10305. https://doi.org/10.1029/2011JA016480

Skjæveland, Å., Moen, J., & Carlson, H. C. (2014). Which cusp upflow events can possibly turn into outflows? *Journal of Geophysical Research: Space Physics*, *119*, 6876–6890. https://doi.org/10.1002/2013JA019495

Slepian, D. (1978). Prolate spheroidal wave functions, Fourier analysis, and Uncertainty—V: The discrete case. *Bell System Technical Journal*, *57*(5), 1371–1430. https://doi.org/10.1002/j.1538-7305.1978.tb02104.x

Stasiewicz, K., Bellan, P., Chaston, C., Kletzing, C., Lysak, R., Maggs, J., et al. (2000). Small scale Alfvenic structure in the aurora. *Space Science Reviews*, *92*(3–4), 423–533.

Stasiewicz, K., Khotyaintsev, Y., Berthomier, M., & Wahlund, JE. (2000). Identification of widespread turbulence of dispersive Alfvén waves. *Geophysical Research Letters*, *27*(2), 173–176. https://doi.org/10.1029/1999GL010696

Strangeway, R. J., Ergun, R. E., Su, Y., Carlson, C. W., & Elphic, R. C. (2005). Factors controlling ionospheric outflows as observed at intermediate altitudes. *Journal of Geophysical Research*, *110*, A03221. https://doi.org/10.1029/2004JA010829

Su, Y.-J., Caton, R. G., Horwitz, J. L., & Richards, P. G. (1999). Systematic modeling of soft-electron precipitation effects on high-latitude F region and topside ionospheric upflows. *Journal of Geophysical Research*, *104*(A1), 153–163. https://doi.org/10.1029/1998JA900068

Thomson, D. J. (1982). Spectrum estimation and harmonic analysis. *Proceedings of the IEEE*, *70*(9), 1055–1096.

van der Meeren, C., Burrell, A. G., & Laundal, K. M. (2018). apexpy: Apexpy version 1.0.3. http://doi.org/10.5281/zenodo.1214207

Varney, R. H., Wiltberger, M., Zhang, B., Lotko, W., & Lyon, J. (2016). Influence of ion outflow in coupled geospace simulations: 1. Physics-based ion outflow model development and sensitivity study. *Journal of Geophysical Research: Space Physics*, *121*, 9671–9687. https://doi.org/10.1002/2016JA022777

Waara, M., Slapak, R., Nilsson, H., Stenberg, G., André, M., & Barghouthi, I. A. (2011). Statistical evidence for O+ energization and outflow caused by wave-particle interaction in the high altitude cusp and mantle. *Annales Geophysicae*, *29*(5), 945–954.

Wahlund, J.-E., Eriksson, A. I., Holback, B., Boehm, M. H., Bonnell, J., Kintner, P. M., et al. (1998). Broadband ELF plasma emission during auroral energization: 1. Slow ion acoustic waves. *Journal of Geophysical Research*, *103*(A3), 4343–4375. https://doi.org/10.1029/97JA02008

Watermann, J., Stauning, P., Lühr, H, Newell, P. T., Christiansen, F., & Schlegel, K. (2009). Are small-scale field-aligned currents and magnetosheath-like particle precipitation signatures of the same low-altitude cusp? *Advances in Space Research*, *43*(1), 41–46.

Welling, D. T., André, M., Dandouras, I., Delcourt, D., Fazakerley, A., Fontaine, D., et al. (2015). The Earth: Plasma sources, losses, and transport processes. *Space Science Reviews*, *192*, 145–208.

Wilson, G. R., Ober, D. M., Germany, G. A., & Lund, E. J. (2004). Nightside auroral zone and polar cap ion outflow as a function of substorm size and phase. *Journal of Geophysical Research*, *109*, A02206. https://doi.org/10.1029/2003JA009835

Yau, A. W., & André, M (1997). Sources of ion outflow in the high latitude ionosphere. *Space Science Reviews*, *80*, 1–25.

Yau, A. W., Beckwith, P. H., Peterson, W. K., & Shelley, E. G. (1985). Long-term (solar cycle) and seasonal variations of upflowing ionospheric ion events at DE 1 altitudes. *Journal of Geophysical Research*, *90*(A7), 6395–6407. https://doi.org/10.1029/JA090iA07p06395

Yau, A. W., Peterson, W. K., & Shelley, E. G. (1988). Quantitative parametrization of energetic ionospheric ion outflow, *Modeling magnetospheric plasma*, Geophysical Monograph Series (Vol. 44, pp. 211–217). Washington, DC: American Geophysical Union. https://doi.org/10.1029/GM044p0211

Zhang, B., Brambles, O., Lotko, W., Smith, R., Wiltberger, M., & Lyon, J. (2013). Predicting the location of polar cusp in the Lyon-Fedder-Mobarry global magnetosphere simulation. *Journal of Geophysical Research*, *118*, 6327–6337. https://doi.org/10.1002/jgra.50565

Zhang, B., Lotko, W., Brambles, O., Xi, S., Wiltberger, M., & Lyon, J. (2014). Solar wind control of auroral Alfvénic power generated in the magnetotail. *Journal of Geophysical Research: Space Physics*, *119*, 1734–1748. https://doi.org/10.1002/2013JA019178

Zhang, Q.-H., Zong, Q.-G., Lockwood, M., Heelis, R. A., Hairston, M., Liang, J., et al. (2016). Earth's ion upflow associated with polar cap patches: Global and in situ observations. *Geophysical Research Letters*, *43*, 1845–1853. https://doi.org/10.1002/2016GL067897

Zheng, Y., Moore, T. E., Mozer, F. S., Russell, C. T., & Strangeway, R. J. (2005). Polar study of ionospheric ion outflow versus energy input. *Journal of Geophysical Research*, *110*, A07210. https://doi.org/10.1029/2004JA010995

Zhou, X. W., Russell, C. T., Le, G., Fuselier, S. A., & Scudder, J. D. (2000). Solar wind control of the polar cusp at high altitude. *Journal of Geophysical Research*, *105*(A1), 245–251.